

Cosmic Voids in Generated N-body Simulations

Olivia Curtis,^{1*} Tereasa G. Brainerd,¹ Anthony Hernandez²

¹*Department of Astronomy & Institute for Astrophysical Research, Boston University, Boston, MA 02215, USA*

²*Department of Computer Science and Engineering, University of South Florida, Tampa, FL 33620, USA*

Accepted XXX. Received YYY; in original form ZZZ

ABSTRACT

A Generative Adversarial Network (GAN) was used to investigate the statistics and properties of voids in Λ CDM universes. A total of 15,000 2D images, extracted from N-body simulations, were used to train the GAN, which was then used to generate 15,000 novel 2D images. The total number of voids and the distribution of void sizes is similar in both sets of images. However, the generated images yield somewhat fewer small voids than do the simulated images. In addition, the generated images yield far fewer voids with central density contrast ~ -1 . Because the generated images yield fewer of the emptiest voids, the distribution of mean interior density contrast is systematically higher for the generated voids than it is for the simulated voids. The mean radial underdensity profiles of the largest voids are similar in both sets of images, but systematic differences are apparent. On small scales ($r < 0.5r_v$), the underdensity profiles of the voids in the generated images exceed those of the voids in the simulated images. On large scales ($r > 0.5r_v$), the underdensity profiles of the voids in the generated images exceed those of the voids in the simulated images. The discrepancies between the void properties in the two sets of images are likely attributable to systematic difficulties faced by deep learning techniques, such as neural networks struggling to capture absolute patterns in the data.

Key words: methods: numerical – methods: statistical – dark matter – large-scale structure of Universe

1 INTRODUCTION

Galaxies in the universe are distributed within an interconnected, large-scale network of walls and filaments that stretch for hundreds of megaparsecs. Between these structures lie vast, underdense regions of space known as voids. Voids can reach up to $100h^{-1}$ Mpc in diameter (see, e.g., Giovanelli & Haynes 1991 and references therein), and they have the potential to serve as excellent laboratories for testing the popular Λ Cold Dark Matter (Λ CDM) model of structure formation. Due to their underdense nature, voids are dominated by dark energy and they are only weakly influenced by the non-linear effects of gravity. Because of this, the shapes and distributions of voids provide tests of modified theories of gravity, as well as constraints on the dark energy equation of state, inflationary models, and the sum of the neutrino masses (see, e.g., Li et al. 2012, Clampitt et al. 2013, Sahlén 2019, Cai et al. 2015, Falck et al. 2018).

Existing void catalogs (e.g., Hoyle & Vogeley 2004, Sánchez et al. 2016, Mao et al. 2017) suffer from small number statistics since they are insufficiently deep to fully sample cosmic structure on the largest scales. For example, Sánchez et al. (2016) identified only 87 voids in the first 139 sq. degrees of the Dark Energy Survey (e.g., Dark Energy Survey Collaboration, & Flaugher 2005). The relatively small number of voids in current observational catalogs limits our ability to place strong observational constraints on fundamental statistics such as void frequency and mean void radius. However, upcoming surveys from the Vera C. Rubin Observatory, as well as the Nancy Grace

Roman and *Euclid* satellites, are expected yield exceptionally deep maps that will sample structure in the universe on gigaparsec scales. This should yield significant improvements in our understanding of the properties of voids in the observed universe.

From the standpoint of large-scale structure theory, gigaparsec-scale simulations are required in order to determine whether Λ CDM is able to successfully reproduce the largest structures in the universe. While Gpc-scale N-body mock catalogs do exist (e.g., Kim et al. 2011, Falck et al. 2021), the largest voids are so rare that only a few dozen of these objects are found within a single Gpc-scale simulation. N-body simulations of this size are computationally expensive to run, making it challenging to use these types of mock catalogs to fully investigate the statistics of the largest voids in Λ CDM universes. In order to make progress on the theoretical properties of the largest voids, it would be helpful to be able to use a modeling technique that is capable of quickly producing independent, novel catalogs of large-scale structure. One technique that may prove advantageous for such applications is the use of Generative Adversarial Networks (GANs).

GANs originate within the deep learning community and they have already begun to demonstrate their usefulness for astrophysical applications. For example, Rodríguez et al. (2018) used GANs to generate novel 2D images of large-scale structure up to scales of $500h^{-1}$ Mpc. Similarly, Feder et al. (2020) and Curtis & Brainerd (2020) showed that GANs are capable of generating novel 3D density maps of the large-scale structure on megaparsec scales. Kodi Ramanah et al. (2020) experimented with the optimization of a network architecture that could generate 3D density maps in boxes with sidelength

* E-mail: amcurtis@bu.edu

$500h^{-1}$ Mpc. In addition, [Mustafa et al. \(2019\)](#) used GANs to produce novel weak lensing convergence maps, [Schawinski et al. \(2017\)](#) used GANs to recover features in Hubble Space Telescope images beyond the deconvolution limit, [Gan et al. \(2021\)](#) demonstrated the ability to eliminate the effects of seeing on images obtained with the Subaru telescope, and [Zingales & Waldmann \(2018\)](#) showed that GANs can be used to retrieve the spectra of exoplanet atmospheres (allowing computationally expensive Bayesian analyses to be bypassed).

In order for GANs to develop into computationally inexpensive alternatives to enormous, Gpc-scale N-body simulations, they must first demonstrate the ability to reproduce the large-scale structure that is consistently produced by smaller, more typical N-body simulations. In this paper we focus on the statistics and properties of voids in Λ CDM universes, and we compare results obtained from N-body simulations to results obtained from a suitably trained GAN. The paper is organized as follows. In §2, we discuss our computational methods. These include the N-body simulations that were used to train the GAN and the details of the particular GAN that we adopted. We also discuss the network architecture and optimisation of the network weights. In §3 we discuss the underdensity probability function, the *voidfinder* algorithm and various void properties. A discussion of our results is presented in §4. Throughout, we adopt the following cosmological parameters: $h = 0.7$, $\Omega_\Lambda = 0.7$, $\Omega_{m0} = 0.3$, and $\sigma_8 = 0.9$.

2 METHODS

2.1 N-body Simulations

Before a GAN can be used to generate novel density maps of Λ CDM universes, it first must be taught the properties that are expected for the large-scale structure. Teaching the GAN these expected properties is a process known as “training”. Training the GAN requires a set of independent N-body simulations, the results of which allow the GAN to learn the expected properties of the large-scale structure and then to extrapolate from its training in order to produce new images. Here, the training set consisted of ten Λ CDM simulations. Each simulation adopted a cubical box with periodic boundary conditions, a box length of $L = 512h^{-1}$ Mpc, and a total of 512^3 dark matter particles of mass $m_p = 8.3 \times 10^{10} h^{-1} M_\odot$. A unique set of initial conditions for each simulation was generated using N-GenIC¹ ([Springel et al. 2005](#)) and the well-tested Gadget-2² code ([Springel 2005](#)) was used to evolve the simulations from redshift $z = 50$ to the present epoch. All simulations were run on the Shared Computing Cluster at the Massachusetts Green High-Performance Computing Center.

To create a training set for the GAN, 15,000 2D images were extracted from the N-body simulations using the method adopted by [Rodríguez et al. \(2018\)](#). First, each simulation was divided each into 1,000 slices along each of the three primary axes. Each slice was then pixellated using a nearest neighbor mass assignment scheme and 500 non-consecutive slices along each axis were selected. Lastly, each image was smoothed with a Gaussian filter with a width of 1 pixel.

Before being passed to the GAN for training, the density maps from the N-body simulations must be normalized. This is necessary because normalizing reduces the cost of transforming the latent space distribution into the space expected of the true data distribution.

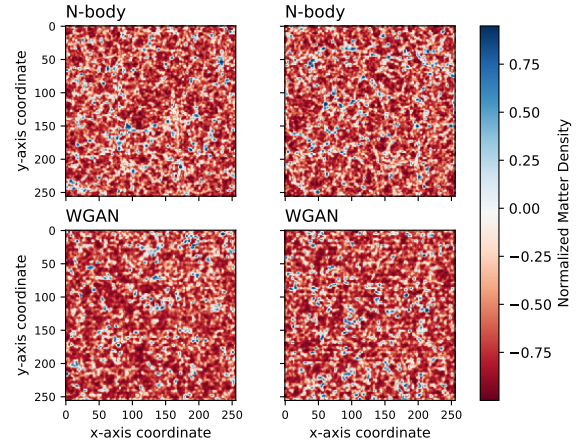


Figure 1. Examples of normalized matter density maps at redshift $z = 0$. Each image has a sidelength of $512h^{-1}$ Mpc and a thickness of $0.512h^{-1}$ Mpc. *Top:* Images obtained from N-body simulations. *Bottom:* Images obtained from a trained Wasserstein GAN (WGAN). Here the local matter density has been normalized to the range $[-1,1]$ using Equation 1 (see text). A full colour version of this figure is available in the online journal.

Following [Rodríguez et al. \(2018\)](#), the density maps from our N-body simulations were normalized into the range $[-1,1]$ using

$$s(x) = \frac{2x}{x+a} . \quad (1)$$

Here, a is an integer that controls the median pixel value of the normalized map and the properties of $s(x)$ resemble those of a logarithm function. For consistency with [Rodríguez et al. \(2018\)](#) we adopt $a = 4$ throughout. Examples of normalized 2D mass density images obtained from the N-body simulations are shown in the top panels of Figure 1.

2.2 Generative Adversarial Networks

A GAN is a game between two deep convolutional neural networks: a discriminator network (D) and a generator network (G). The discriminator, $D : (\vec{x}, \theta_D) \rightarrow [0; 1]$, attempts to label a sample, \vec{x} , as being either ‘real’ or ‘fake.’ Here, ‘real’ means \vec{x} is drawn from the true data distribution (p_{data}) and ‘fake’ means \vec{x} is a generated image drawn from the set of generated data (p_{gen}). The variable θ_D represents the hyper-parameters that characterize D . The generator network, $G : (\vec{z}, \theta_G) \rightarrow \vec{x}$, attempts to map a random variable, \vec{z} , to a sample \vec{x} that appears to be drawn from p_{data} . The random variable is drawn from a latent prior space, $p_{prior}(\vec{z})$, which is generally taken to be a Gaussian.

The discriminator network is trained to maximize the probability of correctly labelling samples that are drawn from the training set and samples that are drawn from the generator network. Meanwhile, the generator network is trained to minimize $\log_{10}(1 - D(G(\vec{z})))$; i.e., the probability of the generator network producing a sample that the discriminator network mislabels as ‘real’. Formally, D and G play what is known as the two-player minimax game:

$$\min_G \max_D [L(G\theta_G, D\theta_D)] \quad (2)$$

¹ <https://www.h-its.org/2014/11/05/ngenic-code/>

² <https://wwwmpa.mpa-garching.mpg.de/gadget/>

with loss function

$$L(G_{\theta_G}, D_{\theta_D}) := \mathbb{E}_{\vec{x} \sim p_{data}(\vec{x})} [\log_{10} D_{\theta_D}(\vec{x})] + \mathbb{E}_{\vec{z} \sim p_{prior}(\vec{z})} [\log_{10}(1 - D_{\theta_D}(G_{\theta_G}(\vec{z})))] \quad (3)$$

where \mathbb{E} is the expectation function. (Note: Equation 3 reduces to the Jensen-Shannon divergence between p_{data} and p_{gen} ; see Goodfellow et al. 2020.)

2.2.1 Wasserstein GANs

For our work, we adopted a particular type of GAN known as a Wasserstein GAN. The motivation for this choice stems from the phenomenon of mode collapse. Mode collapse is said to have occurred in a generative network when the generator produces only one particular output. This happens when the generator discovers one output that consistently deceives the discriminator, at which point the generator stops learning. For example, suppose a GAN is being trained to generate pictures of rooms that would typically be found in a house (see, e.g., Gulrajani et al. 2017). If the generator stops learning after it discovers that one particular generated image of a bathroom consistently deceives the discriminator, mode collapse occurs and the GAN will simply continue to generate that same image of the bathroom as its sole output.

Wasserstein GANs mitigate the problem of mode collapse by adopting what is known as an ‘Earth mover’s distance’ loss function (see, e.g., Arjovsky et al. 2017). In general, the loss function is a function that accumulates error, and the network attempts to optimize the loss function during the training process. The error is distributed to the network’s weights, allowing training to occur. An intuitive explanation of the Earth mover’s distance is found in its name. Imagine trying to relocate a pile of dirt from one location to another. The Earth mover’s distance is then the metric that provides the most cost effective way to transport the dirt.

When applied to GANs, the Earth mover’s distance allows the generator to find the most efficient way of transforming p_{gen} into p_{data} . In return, the discriminator network now scores the ‘realness’ and ‘fakeness’ of an image (i.e., it scores how well p_{gen} resembles p_{data}). For this reason, Arjovsky et al. (2017) refer to the discriminator network as a ‘critic network’, a terminology that we also adopt in this paper. WGANs address the problem of mode collapse by not rewarding the generator network for its ability to generate a single result that consistently deceives the discriminator network. Instead, the generator network attempts to optimize its ability to produce results that receive a high score of ‘realness’ from the critic network.

Additional discussion of Wasserstein GANs and the Earth Mover’s distance is given in Appendix A.

2.2.2 Adam Optimizer

In order to carry out back propagation, we use a standard Adaptive Moment Optimizer known as *Adam* (see Kingma & Ba 2015). *Adam* is a stochastic gradient descent algorithm that updates the network weights using running averages of the first and second moments of the gradients of the loss function. The *Adam* optimizer is a popular choice for performing stochastic gradient descent because it is computationally efficient and has low memory requirements.

For given a set of parameters, $w^{(t)}$, and a loss function, $L^{(t)}$, at training iteration, t , the weights at the $t + 1$ training iteration are found by first calculating the biased first and second moments using Equations 4 and 5, respectively:

$$m_w^{t+1} \leftarrow \beta_1 m_w^t + (1 - \beta_1) \nabla_w L^t \quad (4)$$

$$v_w^{t+1} \leftarrow \beta_2 v_w^t + (1 - \beta_2) (\nabla_w L^t)^2. \quad (5)$$

Here, $\beta_1, \beta_2 \in [0, 1)$ are the exponential decay rates for the moment estimates, $m_w^{(t)}$ are the biased first moment estimates of the weights at step t , $v_w^{(t)}$ are the biased second moment estimates, and ∇_w is the gradient operator with respect to the network parameters.

Typical values for β_1 and β_2 are 0.9 and 0.999, so if m_w^0 and v_w^0 are initialized to zero, a significant bias towards small values in future updates will occur. This bias can be eliminated (making the moments less sensitive to β_1 and β_2 at early timesteps) by normalizing the β ’s such that $\sum_{i=0}^t \beta^i = \frac{1 - \beta^{t+1}}{1 - \beta}$. This normalization can then be removed by dividing the first and second moments by $1 - \beta^{t+1}$ in Equations 6 and 7 below:

$$\hat{m}_w = \frac{m_w^{t+1}}{1 - \beta_1^{t+1}} \quad (6)$$

$$\hat{v}_w = \frac{v_w^{t+1}}{1 - \beta_2^{t+1}}. \quad (7)$$

Finally, the weights at step $t + 1$ are calculated from the unbiased moments using

$$w^{t+1} \leftarrow w^t - \alpha \frac{\hat{m}_w}{\sqrt{\hat{v}_w + \epsilon}}, \quad (8)$$

where α is the algorithm’s learning rate and ϵ is a small number that is used to prevent division by zero. Table 1 lists the values of the hyperparameters that we adopted for our work.

2.2.3 Network Architecture

Throughout, we used a standard WGAN architecture with deep convolutional layers. Details of the architecture are summarized in Table 2. The critic takes a monochromatic image of size 256×256 pixels as its input. Four 2D convolutional layers then down-sample the image. The output of the critic is a score in the range $(-1, 1)$, which describes how ‘real’ (-1) or ‘fake’ ($+1$) the critic thinks the image is. For the convolutional layers, a 4×4 pixel kernel with a stride of size $(2, 2)$ is used. In addition, the inputs of the network are batch normalized before each mini-batch update. The first four convolutional layers have a Leaky Rectified Linear Unit (Leaky-ReLU) activation function, and the last layer has a linear activation function. The first hidden layer down-samples the monochromatic image into a tensor of shape $128 \times 128 \times 64$, where the last dimension is the number of channels. Each consecutive hidden layer then doubles the number of channels to 128, 256, and 512 respectively.

The generator takes a random 1D Gaussian vector of length 200 as its input. The first hidden layer is a linear layer that reshapes the latent space vector into a tensor of shape $16 \times 16 \times 512$ (i.e., 512 low resolution images of size 16×16 pixels). Four 2D convolutional transpose layers up-scale the image while reducing the number of channels. The first four layers use a ReLU activation function and have their inputs batch normalized before each mini-batch update. The output of the generator is a monochromatic image of size 256×256 pixels where each pixel is cast into the range $(-1, 1)$ using a hyperbolic tangent function. To initialize the weights of the critic and generator, a Glorot weight initialization (see, e.g., Glorot & Bengio 2010) was used.

The networks were implemented using Python’s TensorFlow³

³ <https://www.tensorflow.org/>

Table 1. Hyperparameters used in the *Adam* optimizer, as well as other important network parameters (see Table 2).

Hyperparameter	Value	Description
Batch Size	16	Number of training samples fed into the network before back propagation
\mathbf{z} dimension	200	Dimension of the random Gaussian vector
α_D	1e-6	Learning rate for the discriminator's (D) <i>Adam</i> optimizer
$\beta_{1,D}$	0.5	First exponential decay rate for D's <i>Adam</i> optimizer
$\beta_{2,D}$	0.999	Second exponential decay rate for D's <i>Adam</i> optimizer
α_G	5e-5	Learning rate for the generator's (G) <i>Adam</i> optimizer
$\beta_{1,G}$	0.5	First exponential decay rate for G's <i>Adam</i> optimizer
$\beta_{2,G}$	0.999	Second exponential decay rate for G's <i>Adam</i> optimizer
α	0.8	Momentum used in batch normalization
n_{disc}	5	Number of times D is updated for every G update
c	0.01	Weight clipping parameter used to uphold Lipschitz continuity in WGAN architectures
$\alpha_{LeakyReLU}$	0.2	Negative slope coefficient for LeakyReLU activation functions

Table 2. WGAN network architecture used in this paper.

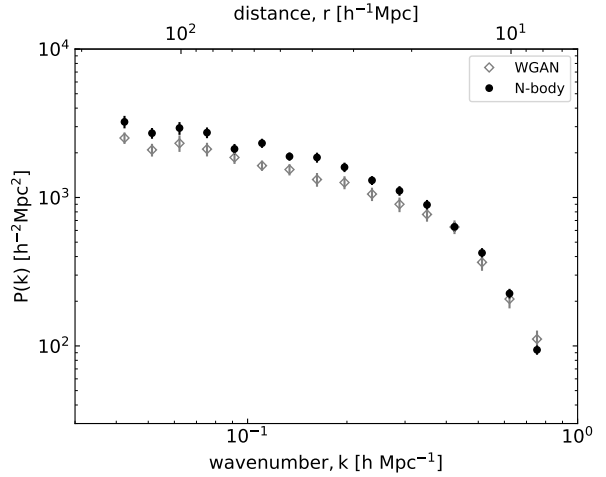
Layer	Operation	Output	Dimension
Critic			
\mathbf{X}			256 x 256 x 1
D_0	Conv2D	LeakyReLU-BatchNorm	128 x 128 x 64
D_1	Conv2D	LeakyReLU-BatchNorm	64 x 64 x 128
D_2	Conv2D	LeakyReLU-BatchNorm	32 x 32 x 256
D_3	Conv2D	LeakyReLU-BatchNorm	16 x 16 x 512
D_4	Linear	Linear	1
Generator			
\mathbf{Z}			200 x 1
G_0	Linear	ReLU-BatchNorm	16 x 16 x 512
G_1	Conv2DTranspose	ReLU-BatchNorm	32 x 32 x 256
G_2	Conv2DTranspose	ReLU-BatchNorm	64 x 64 x 128
G_3	Conv2DTranspose	ReLU-BatchNorm	128 x 128 x 64
G_4	Conv2DTranspose	Tanh	256 x 256 x 1

package (e.g., [Oliphant 2007](#); [Abadi et al. 2016](#)) and were trained on two NVIDIA Tesla P100 graphics processing units with compute capability 6.0. The critic and generator networks had 2.89 million and 16.00 million trainable parameters, respectively. Training was carried out with Python version 3.7.7, TensorFlow version 1.15.0, CUDA version 10.0, and NVIDIA cuDNN version 7.6, and took approximately four hours for 20 training epochs. The implementation of the WGAN described in this paper is available on the first author's GitHub page.⁴

3 RESULTS

The WGAN was trained for 20 epochs and the network parameters were saved after each training epoch. After 20 epochs, the outputs of each saved network were analyzed to determine which training epoch produced matter power spectra that were most similar to the training set. In the case of our WGAN, we found this to occur after four training epochs. This network was then used to generate a set of 15,000 images which were used for the analyses we present below. Two of these generated images are shown in the bottom panels of Figure 1.

Figure 2 shows the results for the matter power of spectra of our simulated and generated datasets. The power spectra were calculated in the standard way (see, e.g., [Davis et al. 1985](#)) and they encompass distance scales that are typical of void sizes (i.e., 10 – 100 h^{-1} Mpc). Points in Figure 2 show the mean power spectra, computed using all

**Figure 2.** Mean matter power spectra, $P(k)$, computed from 15,000 simulated images (circles) and 15,000 images generated with a WGAN (diamonds). Error bars were computed using 10,000 bootstrap resamplings of the data.

simulated and generated images, and error bars were obtained from 10,000 bootstrap resamplings of the data. From Figure 2, $P(k)$ from the generated images agrees with $P(k)$ from the simulated images on scales $< 20 h^{-1}$ Mpc. On larger scales, however, the generated images yield systematically lower values of $P(k)$ than do the simulated images.

3.1 Underdensity Probability Function

In the observed universe, the Void Probability Function (VPF) is commonly used to determine whether a randomly selected region in an image is devoid of galaxies (e.g., [White 1979](#); [Lachieze-Rey et al. 1992](#); [Vogeley et al. 1994](#)). The VPF depends on the galaxy N -point correlation function via

$$P_0(N, A) = \exp \left[\sum_{N=1}^{\infty} \frac{(-n)^N}{N!} \int_A w_N(\vec{x}_1, \dots, \vec{x}_N) d^2x_1 \dots d^2x_N \right] \quad (9)$$

(e.g., [White 1979](#)), where n is the average number density of galaxies in the field, w_N are the N -point correlation functions, and \vec{x}_i are the i -th galaxy positions in the area A .

Because our GAN outputs consist of images of a smoothed mass density distribution (i.e., not the locations of individual galaxies

⁴ <https://github.com/o-curtis/>

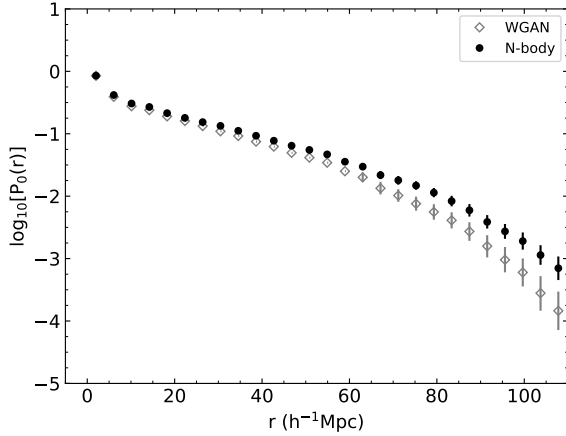


Figure 3. Mean underdensity probability function for images obtained from N-body simulations (circles) and WGAN-generated images (diamonds). Error bars were computed from 10,000 bootstrap resamplings of the data and are omitted when they are comparable to or smaller than the data points.

or individual particles) we do not compute the VPF. Instead, we compute a similar statistic known as the Underdensity Probability Function (UPF). The UPF measures the probability that, within an area of radius r , a randomly selected region of space is less dense than some particular threshold density. To identify underdense regions in our simulated and generated images, we define a normalized density contrast $\Delta \equiv \frac{\delta\rho}{\rho}$ and we adopt a threshold for the mass density contrast of $\Delta < -0.6$. Here ρ is the local matter density and $\delta\rho$ is the difference between the local matter density and mean matter density of the image. That is, the UPF is defined as $U(r) = P(\Delta < \Delta_{\text{crit}}; r)$ where $\Delta_{\text{crit}} = -0.6$.

The UPF for the simulated and generated images was determined by computing the mean mass density contrast within randomly-placed circles of radius r . If the average density contrast within a circle of radius r is less than Δ_{crit} , then that particular region qualifies as being sufficiently underdense to be included in the calculation of the UPF. A total of $N_{\text{test}} = 10^4$ random circles of radius r were placed within each image and the total number of underdense regions, N_0 , was then computed. The UPF was then defined as $U(r) = N(0; \Delta < \Delta_{\text{crit}}) / N_{\text{test}}$.

Figure 3 shows the mean UPF obtained from 15,000 simulated images and 15,000 generated images. The UPFs were calculated following the steps described above and error bars were calculated by bootstrap resampling of both sets of distributions. Note that, since smaller circles in an image are encompassed by larger circles in the same image, the data points in Figure 3 are not independent of one another. Hence, the point-to-point scatter is considerably smaller than the formal, bootstrapped error bars. Similar to the power spectra, there is good agreement between the simulated and WGAN images on small scales. On larger scales, there is a significantly lower chance of finding underdense regions in the generated data than in the simulated data, with the difference increasing for regions $\geq 60h^{-1}$ Mpc.

3.2 Void Identification

To identify voids in both the simulated and generated density fields, we adopted a *voidfinder* algorithm that is similar to the algorithm

used by El-Ad & Piran (1997) and Hoyle & Vogeley (2004) to identify voids in catalogs of galaxies. When applied to an observational dataset, the *voidfinder* algorithm identifies voids using the observed locations of galaxies. In our case there are no galaxies in the images. Instead, the images consist of pixels with known values of the mass density. Our version of the *voidfinder* algorithm, therefore, scans images of the large-scale structure as defined by the pixellated mass density. The algorithm yields a set of individual void centres and a list of which pixels in a given image belong to which voids.

Our *voidfinder* algorithm can be summarized in four steps: [1] each pixel is classified as being either a ‘wall pixel’ or a ‘void pixel’, [2] the distance between every void pixel and the nearest wall pixel is calculated, [3] void centres are defined to be the locations of the most isolated void pixels (i.e., the void pixels that are farthest from a wall pixel), and [4] as part of the process of identifying underdense regions that are interconnected, the areas of the larger voids are ‘enhanced’ to include overlapping regions of low mass density. The first step is performed by scanning over every pixel in the image using a circular aperture of radius $d = 3$ pixels that takes the periodic boundary into account. If the pixel that the circular aperture is centred on contains at least $N = 9$ pixels with a normalised density contrast > -0.6 , the pixel is classified as a ‘wall pixel’. That is, if $\sim d^2$ of the pixels in the neighbourhood around the central pixel are sufficiently dense compared to the mean, the central pixel is classified as a wall pixel. Any pixel that is not classified as a wall pixel is classified as a ‘void pixel.’ The second step is to iterate over each void pixel and determine its distance to the nearest wall pixel. This is done by finding the circle of maximum radius that can be centred around each void pixel such that the circle contains no wall pixels. Following the terminology of Hoyle & Vogeley (2004), we refer to these maximal circles as ‘holes’.

Once all of the pixels have been classified as being either a void pixel or a wall pixel, the void centres are then identified. To do this, we begin by sorting all holes in a given image from largest to smallest in terms of their radii. We then define the centre of the largest hole in the image to be the centre of the first void. Having found this first void centre, we then iterate over all holes. If the next hole in the sorted list overlaps with any previously-identified void by more than 10% of its own area, that hole is not considered to be an individual void and, at this point, is temporarily ignored. If the next hole in the sorted list does not overlap with any previously-identified void (or if the overlap is $\leq 10\%$ of its own area), the hole is classified as distinct void, with the centre of the hole being the void centre. This process continues until all holes with radius > 3 pixels have been considered.

In order to account for the fact that underdense regions of space are interconnected, the final step in the process of identifying the voids is to consider the degree of overlap between holes and voids. The process is intended to examine the underdense regions near the edges of the holes and either assign those underdense regions to appropriate voids or reject them as being part of a void. If a hole overlaps a single void by $> 50\%$ of its own area, then we consider the hole to be part of the void. If a hole overlaps multiple voids by $> 50\%$ of its own area, we consider it to be part of the largest overlapping void. If a hole overlaps a void by $\leq 10\%$ of its own area, then the hole is identified as a distinct void, but the area of overlap is assigned to the larger void. If the overlap between a hole and a void is $> 10\%$ of the hole’s area but $< 50\%$, the pixels in the hole are not assigned to any void. By this process, the total areas of the larger voids are enhanced relative to the areas of the maximal circles that are centred on the void centres.

Figure 4 shows the results of the *voidfinder* algorithm as applied to a single image. The different panels of Figure 4 show: a) the normalised density contrast, b) the locations of wall pixels (white)

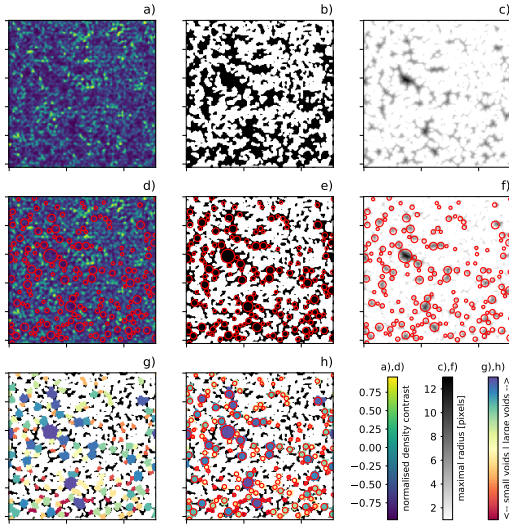


Figure 4. Illustration of the *voidfinder* algorithm. a) Normalised mass density. b) Locations of wall pixels (white) and void pixels (black). c) Maximal radius for each void pixel. d) – f) Largest hole contained within each void, overlaid on the panels directly above (red circles). g) Final void areas overlaid on the wall/void pixel distribution. h) Same as (g), but with the largest hole contained within each void superposed on the image. A full colour version of this figure is available in the on-line journal.

and void pixels (black), c) the distance to the nearest wall pixel at each location (i.e., the maximal radius for each pixel), d) the largest holes (i.e., the circles that define the void centres) overlaid on the density contrast, e) the largest holes overlaid on the wall/void pixel image, f) the locations of the largest holes overlaid on the distance to the nearest wall pixel, g) the final void areas overlaid on the wall/void pixel image, and h) same as (g), but with the largest holes indicated. The 15,000 images from the N-body simulations yielded a total of 2.5 million voids and the 15,000 generated images yielded a total of 2.8 million voids.

3.3 Void Properties

Below we will adopt the following terminology when discussing the void properties. The ‘radius’ of a void is simply the radius of the void’s maximal circle (i.e., the largest circle, centred on the void centre, with radius equal to the distance to the nearest wall pixel). The ‘effective radius’ of a void corresponds to the radius of a circle that, after the area of the void has been adjusted for any overlaps, is equal to the final area assigned to the void. Since some of the smaller voids lose area to neighbouring large voids, their effective radii will be less than the radii of their maximal circles. Conversely, the larger voids with areas that have been enhanced by the addition of pixels from neighbouring small voids (or significantly overlapping holes) will have effective radii that are larger than the radius of their maximal circle.

The top panels of Figure 5 show normalised probability distributions for: a) the void radii and b) the effective void radii. Overall there is good agreement between the results for the simulated and generated images. Compared to the simulated images, however, the generated

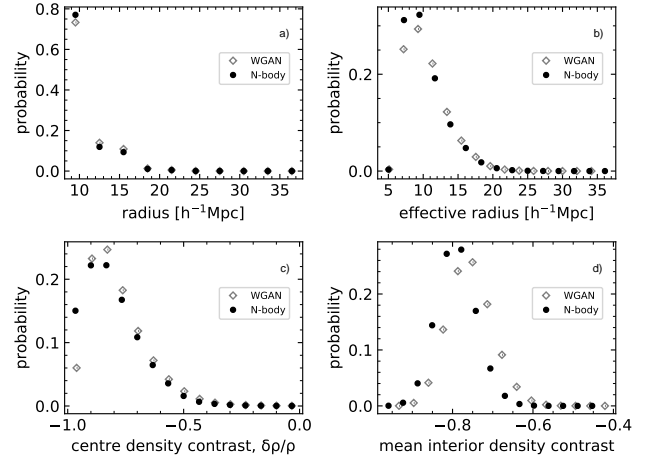


Figure 5. Normalized probability distributions of various void properties. a) Void radii. b) Void effective radii. c) Value of the density contrast at the centres of the voids. d) Mean interior density contrast, computed using the final areas of the voids. Error bars are omitted because they are comparable to or smaller than the sizes of the data points.

images produce fewer of the smallest voids. The median void radius in the generated images is identical to that of the simulated images ($10.0h^{-1}$ Mpc), but the median effective void radius in the generated images ($10.0h^{-1}$ Mpc) is somewhat larger than that in the simulated images ($9.6h^{-1}$ Mpc). Figure 5c) shows the normalised probability distributions for the density contrast at the centres of the voids. Here, again, the distributions are similar and the median value of the central density contrast is nearly identical for the simulated and generated images (-0.83 in the simulated images vs. -0.81 in the generated images). However, compared to the simulated images, the generated images produce far fewer voids for which the central density contrast is ~ -1 (i.e., the most underdense void centres). Conversely, the generated images produce somewhat more voids with central density contrasts between ~ -0.9 and ~ -0.5 than do the simulated images. Figure 5d) shows the normalised probability distributions for the mean density contrast within the voids. While the median values of the distributions in Figure 5d) are similar (-0.79 for the simulated images vs. -0.76 for the generated images), there is a clear offset between the two distributions such that the mean density contrast of the generated voids is systematically higher than that of the simulated voids.

For the remainder of our analyses we will focus on a comparison of the best-resolved voids. These are the largest voids in the images, and here we will restrict the analysis to only those voids with radii ≥ 10 pixels (corresponding to a radius $\geq 20h^{-1}$ Mpc). Because large voids are rare, these represent only a small fraction of the total number of voids in the samples (15,063 in the simulated sample and 16,165 in the generated sample). However, unlike the smallest voids which are poorly resolved, these largest voids are sufficiently well resolved to allow a computation of their radial density profiles.

For comparison with our complete samples of voids shown in Figure 5, Figure 6 shows the same normalised probability distributions, but using only the largest voids. Compared to the results in Figure 5, there is a much greater difference between the distributions of void radii and void effective radii in Figure 6. This is due to a combination of two effects that go into assigning each void its final area (from which the effective radius is determined). First, the larger holes have

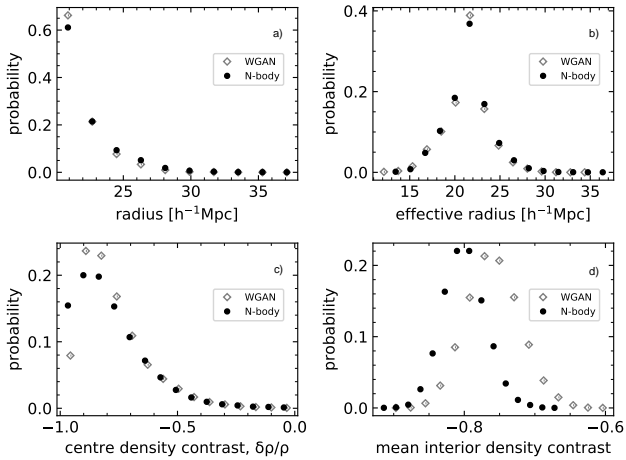


Figure 6. Same as Figure 5, but here only voids with radius $\geq 20h^{-1}$ Mpc are used.

a larger number of underdense pixels just outside their circumferences than do the smaller holes. Therefore, a large hole that has been identified as being a void has a higher probability of having its final area enhanced relative to the area of the hole (i.e., by the addition of pixels from smaller holes that overlap the large hole by a significant amount). This necessarily increases the effective radius of a void with an enhanced area. In addition, because of their relatively large size, the probability of the largest voids overlapping by a small amount is higher than the probability of the smallest voids overlapping by a similarly small amount. In the case of these small overlaps ($\leq 10\%$ of the area of the smallest of the two associated holes), the overlap area is assigned to the larger void, resulting in the smaller of the two voids having a final area that is reduced compared to the size of its hole (and hence, having an effective radius smaller than the radius of its associated hole). From panels a) and b) of Figure 6, the median values of the void radii ($20.0h^{-1}$ Mpc) and void effective radii ($21.4h^{-1}$ Mpc) are identical in the simulated and generated images.

Figure 6c) shows trends that are similar to those in Figure 5c). While the median central densities of the largest voids are similar in both the simulated and the generated images (-0.82 for the simulated images vs. -0.81 for the generated images), the generated images produce far fewer of the largest voids with central densities ~ -1 . Like the complete void sample, the generated images also produce somewhat more voids with central densities larger than ~ -1 , but the range over which this occurs (~ -0.9 to ~ -0.75) is smaller than in the full sample. Figure 6d) also shows trends that are similar to those in Figure 5d). The median values of the distributions in Figure 6d) are similar (-0.80 for the simulated images vs. -0.76 for the generated images), and there is a clear offset between the two distributions such that the mean density contrast of the largest generated voids is systematically higher than that of the largest simulated voids.

Lastly, Figure 7 shows the mean radial underdensity profiles for the largest voids, plotted in terms of dimensionless distance relative to the void radius, (r/r_v). As expected, the central regions of the voids are extremely underdense and the density contrast increases with radius from the void centres. While the radial underdensity profiles are similar in both the simulated and generated images, there are clear differences. For distances $r \lesssim 0.6r_v$, the underdensities of the generated voids are somewhat higher than the underdensities of the simulated voids. For distances $r \gtrsim 0.6r_v$, the sense of the

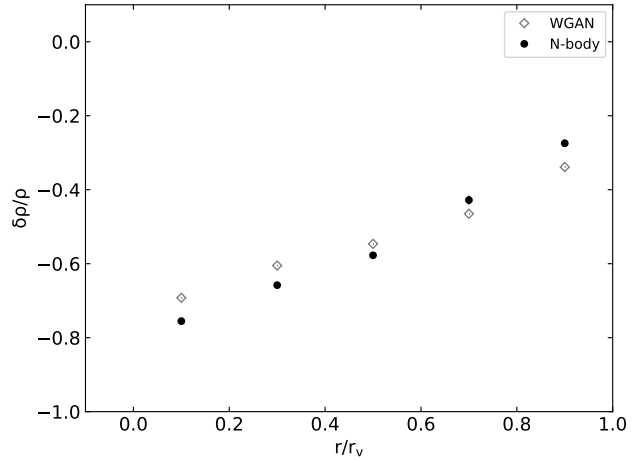


Figure 7. Mean radial underdensity profiles of largest voids, plotted as a function of dimensionless distance relative to the void centres, (r/r_v). Error bars are omitted because they are comparable to or smaller than the data points.

of disagreement reverses, with the underdensities of the generated voids being somewhat lower than the underdensities of the simulated voids.

4 DISCUSSION

We have explored the use of a standard deep convolutional Wasserstein GAN (WGAN) for the purposes of generating novel 2D images of the smoothed mass density field of Λ CDM universes. The WGAN was trained using 15,000 2D images of the large-scale structure that were obtained from N-body simulations. The trained WGAN was used to generate 15,000 2D images and a *voidfinder* algorithm, modified to identify regions of low mass density (as opposed to regions of low galaxy density), was then used to create void catalogs from the simulated and generated images. The simulated and generated images yield a similar number of voids (2.5 million voids in the simulated images vs. 2.8 million voids in the generated images) and the properties of the voids in the simulated and generated images are also similar. Systematic differences between the properties of the simulated and generated voids are, however, apparent. Compared to the simulated images, the generated images yield somewhat fewer of the smallest voids and significantly fewer voids with central density contrast ~ -1 . Overall, the generated images yield fewer of the emptiest voids and, as a result, the distribution of mean interior density contrast for the generated voids is offset systematically from the distribution of mean interior density contrast for the simulated voids.

Neural networks function by learning the average trends in the target distribution but they struggle to capture absolute patterns in the data (see, e.g., Li et al. 2018 for a detailed discussion). That is, our deep convolutional WGAN is clearly able to detect trends in the pixel-to-pixel variations of the smoothed density contrast, but it is not reliably capturing the absolute highs and lows. This effect can be seen in Figures 5c) and 6c), where the WGAN images produce significantly fewer voids with central density contrast ~ -1 than do the simulated images. The failure of the WGAN to reliably capture the absolute highs and lows of the smoothed density contrast also explains the systematic offsets between the distribution of mean

interior density contrast for the generated and simulated images in Figures 5d) and 6d).

GANs present an opportunity to investigate the distribution of large-scale structure on Gpc-scales across multiple epochs of the universe without the need for computationally-expensive Gpc-scale N-body simulations. In order for GANs to become a truly viable alternative to simulations, they need to be able to fully reproduce the structure that is seen in typical N-body simulations. While our WGAN produced voids with properties that were in broad general agreement with the properties of voids in N-body simulations, the systematic differences between the populations are an indication that improvements in the WGAN approach are still necessary.

For future work, the network architecture will need to be optimised in such a way that it allows the trained WGAN to better capture absolute trends in the target images. Such optimisation may be dependent on the size of the convolutional kernels and/or the values of the hyperparameters used in the generator and critic networks. The use of inception blocks (see Szegedy et al. 2015), for example, would help the network to pick up features of varying sizes by scanning the input layer with kernels of varying sizes. This alone might resolve the issue of the centres of the generated voids being insufficiently underdense. Finally, it will be interesting to see whether more sophisticated network architectures, such as the one used by Kodi Ramanah et al. (2020) to generate large-scale structure maps, yield improved results for the statistics of generated voids.

DATA AVAILABILITY

The data underlying this article will be shared on reasonable request to the corresponding author.

REFERENCES

- Abadi M., et al., 2016, in Keeton K., Roscoe T., eds, Proc. of the 12th USENIX Symposium on Operating Systems Design and Implementation. USENIX Association, Berkeley, California, USA, p. 265
- Arjovsky M., Chintala S., Bottou L., 2017, in Precup D., Teh Y. W., eds, Proc. of Machine Learning Research Vol. 70, Proc. of the 34th International Conference on Machine Learning. Journal of Machine Learning Research, Inc., Brookline, Massachusetts, USA, p. 214
- Cai Y.-C., Padilla N., Li B., 2015, *MNRAS*, **451**, 1036
- Clampitt J., Cai Y.-C., Li B., 2013, *MNRAS*, **431**, 749
- Curtis O., Brainerd T. G., 2020, *RNAAS*, **4**, 90
- Dark Energy Survey Collaboration, Flaugher B., 2005, *International Journal of Modern Physics A*, **20**, 3121
- Davis M., Efstathiou G., Frenk C. S., White S. D., 1985, *ApJ*, **292**, 371
- El-Ad H., Piran T., 1997, *ApJ*, **491**, 421
- Falck B., Koyama K., Zhao G.-B., Cautun M., 2018, *MNRAS*, **475**, 3262
- Falck B., Wang J., Jenkins A., Lemson G., Medvedev D., Neyrinck M. C., Szalay A. S., 2021, preprint (arXiv:2101.03631)
- Feder R. M., Berger P., Stein G., 2020, *Phys. Rev. D*, **102**, 103504
- Gan F. K., Bekki K., Hashemizadeh H., 2021, preprint (arXiv:2103.09711)
- Giovanelli R., Haynes M. P., 1991, *ARA&A*, **29**, 499
- Glort X., Bengio Y., 2010, in Teh Y. W., Titterton M., eds, Proc. of Machine Learning Research Vol. 9, Proc. of the Thirteenth International Conference on Artificial Intelligence and Statistics. Journal of Machine Learning Research Inc., Brookline, Massachusetts, USA, p. 249
- Goodfellow I., Pouget-Abadie J., Mirza M., Xu B., Warde-Farley D., Ozair S., Courville A., Bengio Y., 2020, *Communications of the Association for Computing Machinery*, **63**, 139
- Gulrajani I., Ahmed F., Arjovsky M., Dumoulin V., Courville A., 2017, in von Luxburg U., Guyon I., Bengio S., Wallach H., Fergus R., eds, Proc. of the 31st International Conference on Neural Information Processing Systems. Curran Associates Inc., Red Hook, NY, USA, p. 5769
- Hoyle F., Vogeley M. S., 2004, *ApJ*, **607**, 751
- Kim J., Park C., Rossi G., Lee S. M., Gott III J. R., 2011, *Journal of Korean Astronomical Society*, **44**, 217
- Kingma D. P., Ba J., 2015, in Bengio Y., LeCun Y., eds, Proc. of the 3rd International Conference on Learning Representations. International Conference on Learning Representations, San Diego, California, USA, <https://arxiv.org/pdf/1412.6980.pdf>
- Kodi Ramanah D., Charnock T., Villaescusa-Navarro F., Wandelt B. D., 2020, *MNRAS*, **495**, 4227
- Lachieze-Rey M., da Costa L. N., Maurogordato S., 1992, *ApJ*, **399**, 10
- Li B., Zhao G.-B., Koyama K., 2012, *MNRAS*, **421**, 3481
- Li Y., Yu R., Shahabi C., Liu Y., 2018, in Bengio Y., LeCun Y., eds, Proc. of the 6th International Conference on Learning Representations. International Conference on Learning Representations, San Diego, California, USA, <https://openreview.net/forum?id=SJIHXGWAZ>
- Mao Q., et al., 2017, *ApJ*, **835**, 161
- Mustafa M., Bard D., Bhimji W., Lukić Z., Al-Rfou R., Kratochvil J. M., 2019, *Computational Astrophysics and Cosmology*, **6**, 1
- Oliphant T. E., 2007, *Computing in Science & Engineering*, **9**, 10
- Rodríguez A. C., Kacprzak T., Lucchi A., Amara A., Sgier R., Fluri J., Hofmann T., Réfrégier A., 2018, *Computational Astrophysics and Cosmology*, **5**, 4
- Sahlén M., 2019, *Phys. Rev. D*, **99**, 063525
- Sánchez C., et al., 2016, *MNRAS*, p. stw2745
- Schawinski K., Zhang C., Zhang H., Fowler L., Santhanam G. K., 2017, *MNRAS*, **467**, L110
- Springel V., 2005, *MNRAS*, **364**, 1105
- Springel V., et al., 2005, *Nature*, **435**, 629
- Szegedy C., et al., 2015, in Baldwin R., ed., Proc. of the 2015 Institute of Electrical and Electronics Engineers' conference on computer vision and pattern recognition. Institute of Electrical and Electronics Engineers, Los Alamitos, California, USA, p. 1
- Vogelely M. S., Geller M. J., Park C., Huchra J. P., 1994, *AJ*, **108**, 745
- White S. D. M., 1979, *MNRAS*, **189**, 831
- Zingales T., Waldmann I. P., 2018, *AJ*, **156**, 268

APPENDIX A: WASSERSTEIN GAN

Arjovsky et al. (2017) suggest switching the standard GAN loss function to the Wasserstein metric (a.k.a. the Kantorovich–Rubinstein metric or Earth mover’s distance) so that the loss function becomes:

$$W(\mathbb{P}_{data}, \mathbb{P}_{gen}) := \inf_{\gamma(x,y) \in \Pi(\mathbb{P}_{data}, \mathbb{P}_{gen})} \mathbb{E}_{(x,y) \sim \gamma} [|x-y|] \quad (A1)$$

Here, $\Pi(\mathbb{P}_{data}, \mathbb{P}_{gen})$ is the set of all couplings of \mathbb{P}_{data} and \mathbb{P}_{gen} . If each distribution is thought to be a unit amount of soil piled over a metric space, then $\gamma(x, y)$ represents how much soil must be moved from x to y such that \mathbb{P}_{data} becomes \mathbb{P}_{gen} . In other words, Equation A1 reveals the cost of the optimal way to transfer soil.

In practice, solving A1 is intractable. However, Arjovsky et al. (2017) have shown that the Wasserstein metric reduces to

$$W(\mathbb{P}_{data}, \mathbb{P}_{gen}) := -\mathbb{E}_{\vec{z} \sim p_{prior}(\vec{z})} [f(G_{\theta_G}(\vec{z}))] \quad (A2)$$

provided that f exists and is K-Lipschitz. In the WGAN algorithm, f is analogous to the set of weights, w , that parametrise the critic network. In other words, given weights, w , lying in a compact space, W , one back propagates through $\mathbb{E}_{\vec{z} \sim p_{prior}(\vec{z})} [f_w(G_{\theta_G}(\vec{z}))]$ to update the generator’s weights, just as one would do in the standard GAN architecture. However, to ensure the weights lie in W , the weights are clipped to a box $W = [-c, c]$, where c is a clipping parameter.

The training algorithm for a WGAN is similar to the standard GAN algorithm. Aside from the different loss functions and weight

clipping, the only change in the WGAN algorithm is that the critic network has its weights updated an integer times more than the does the generator network (i.e., in the standard GAN architecture, both G and D are updated evenly). This change possible because, unlike the Jensen-Shannon Divergence, the Earth mover's distance is continuous and differentiable everywhere, and allows the critic to train until optimality is reached.

Allowing the critic to train until optimality is reached makes mode collapse improbable in the WGAN architecture. This is due to the fact that the critic is no longer trained on how well it can discriminate between real and fake images. Rather, the critic is trained on how it scores the realness or fakeness of an image. Training the critic in this way improves network stability by giving the generator better feedback on how to update its weights.

This paper has been typeset from a \TeX/L\AA\TeX file prepared by the author.